# An Independently Controlled Energy Storage to Support Short Term Frequency Fluctuations In Weak Electrical Grids

Charmalee Jayamaha[1,*], Alessandro Costabeber[2], Arthur Williams[3], Mark Sumner[4]

[1]Power Electronics, Machines and Control Group, Faculty of Engineering, The University of Nottingham, University Park, Nottingham, NG7 2RD.
[*]charmalee.jayamaha@gmail.com

**Abstract:** This paper proposes the use of Energy Storage (ES) to support frequency fluctuations in weak grids powered by low-power synchronous generators (SGs). Traditionally, large synchronous generators rely on high inertia and governor control to guarantee the frequency stability of the network. The scenario changes in networks with a large penetration of small distributed generators (DGs) with smaller inertia, where load variations can lead to large frequency deviations, violating the over/under frequency protection limits. The proposed energy storage control injects active power during load transients so that the frequency is constrained within predefined thresholds. The system frequency is detected by a Double Second-Order Generalised Integrator Frequency Locked Loop (DSOGI-FLL), eliminating the need for communication between energy storage and synchronous generator and providing "plug-and-play" capability. The proposed method combined with the continuous speed governing supports the frequency well within the primary frequency transient requirements. The solution has been validated using an $8kW$ laboratory system.

***Key words*:** **Energy Storage Systems, Primary Frequency Control, Weak Grids, DSOGI-FLL, Distributed Generation.**

## 1. Introduction

During the last two decades, the paradigm of power generation has evolved from large centralized power plants towards a more decentralised structure, where small distributed generators (DGs) support the central production. Also, the capacity of DGs is expected to grow rapidly in the next two decades [1]. DGs are characterized by their power rating normally from a few kW to tens of MW, their operation without a central control from the utility and their connection to the distribution network (MV or LV). The motivation for DGs is high, particularly as the environmental need for reducing $CO_2$ emissions [2, 3] has imposed restrictions on fossil fuel based power generation. Distributed generation can lead to low infrastructural costs, energy diversification and deregulation of the energy market and can also reduce distribution losses, as they deliver power close to the loads, increasing the hosting capacity of existing lines.

The integration of DGs in the grid also has challenges, and these must be properly managed [4, 5]. DGs increase fault current levels [6], increasing the cost of protection. Moreover, the relay protection equipment and its control become more complex [7], due to the bi-directional power flow that may occur in the presence of DGs. Nevertheless, from the perspective of fault management, DGs offer an additional degree of freedom: in the event of severe and non-recoverable faults in the main grid, DGs can potentially operate in an island, autonomously feeding essential loads.

Recent discussions on Smart Grids [8, 9] are envisioning new scenarios. One of them is the partitioning of the distribution network in to microgrids (MGs) containing a sufficient number of DGs that are able to operate in grid-connected or islanded modes [10–12]. In this context, DG can be sources connected to the grid using power electronic converters (e.g. PV, wind, battery) or using conventional generators (e.g. biomass, small-wind, hydro). In grid-connected mode, the MG can perform internal optimizations [13], relying on the main grid to guarantee the continuity of the service. In islanded mode, power balance and stability become the priority and severe load transients can drive conventional DGs out of synchronism due to the low system inertia, leading to a partial or total disconnection [14]. Such a scenario may create a weak MG susceptible to voltage and frequency instabilities.

As a solution to stabilize transients in MG, [1] reports the use of the 'virtual synchronous generator'. In this concept, the DG is supported by short term ES together connected to the grid using a power electronic inverter and a proper control method to alleviate transient instabilities in weak MG [15]. The use of ES to support short term frequency deviations in the context of wind farms and MGs is reported in [16–18]. For long term secondary response frequency support, [19] presents a Battery ES (BES) in a rule based control strategy to reduce power losses and to improve grid stability in weak grids connected to utility scale PV systems. Another study in [20] uses virtual and adaptive impedance loops to provide a better frequency response than the traditional secondary frequency response in PV based MGs. A case study is presented in [21], where a MG including renewable energy sources (RES), variable-speed engines and ES has been designed and tested, proving how the availability of ES can help in balancing the dynamics of different sources, easing the operation of the islanded grid with traditional droop methods [22]. A similar approach is presented in [23], which includes a speed-droop controlled synchronous generator in the MG. Other contributions in the literature recognize the role of ES, and extend the concept of ES applied with electronically interfaced sources: both [24] and [25] propose the addition of a STATCOM with ES, coupled to SGs, to compensate for load distortions and unbalances. As pointed out in [23], ES can be added in parallel to a small SG through a three-phase inverter, acting as a reserve of active power able to smooth out load transients. However, a general approach to frequency stability analysis of grid-connected or islanded networks with power electronics [26, 27] and SGs can become unnecessarily complex. This is even more challenging in the context of a weak MG, which can be more susceptible to frequency deviations due to the low system inertia. Thus, considering [1, 15–25], we believe that there is a gap in knowledge and experiments of a robust ES control technique that can work independently but operate hand in hand with the existing prime mover governor frequency control techniques. In this study, we aim to provide such a plug and play ES control technique backed by experimental validation.

This paper proposes a novel and simple control technique to utilise an ES, such that the short term active power support from the ES can limit the sudden frequency variations to remain within given boundaries, during severe load transients. The control method coordinates with the DG's own governor frequency control to prevent harmful frequency excursions by using detected power system frequency as part of its own control; hence, eliminating communication requirements. As a proof-of-concept, the system was developed as an autonomous MG fed by a single grid-forming SG and a Li-ion Battery Energy Storage (BES), which is controlled by the proposed ES control technique.

The rest of the paper is structured as follows. Section II presents the weak grid model used to develop the control system. In Section III, the properties of the proposed ES control system are presented. Concept validation through simulation results and the experimental results is reported in Section IV followed by conclusions in Section V.

## 2. The Weak Grid Model

The MG considered in this paper is illustrated in Fig. 1. The MG is powered by a single DG unit with a generic prime mover. In normal operation, the system frequency is controlled to $50Hz$ by the governor of the prime mover - the speed control loop, is shown in Fig.2. This represents a 'weak-grid' as the load is comparable to the rating, and will cause a significant impact on voltage and frequency when connected. The same system has been emulated in an $8kW$ experimental rig, and the data from the experimental system have been used for the control design presented in the following paragraphs and for the preliminary verification through simulation.

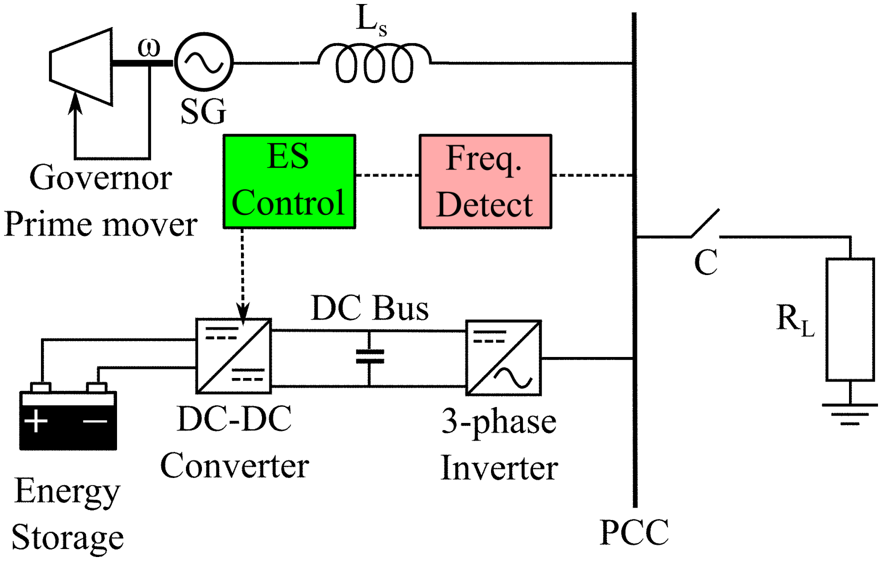

***Fig. 1.*** *Block diagram of the weak grid with ES support*

The speed loop was derived by simplifying and linearising the swing equation around torque, $T(Nm)$ and angular frequency $\omega(rad/s)$ [28]. In this particular scenario, the prime mover does not need droop control. The dynamics of the prime mover are represented by its dominant time constant $\tau_{en}(s)$ as a first order lag and the generator is modelled as a lumped inertia $J(Kgm^2)$ that represents the inertia of the prime mover and the generator combined [29]. The closed loop transfer function (CLTF) can be obtained from Fig.2 as shown in (1). The electrical loading of the system is approximated to a load torque acting directly on the prime mover of the system.

$$G_{CL}(s) = \frac{\omega(s)}{\omega_{ref}(s)} = \frac{(\tau_{en}s + 1)s}{J\tau_{en}s^3 + Js^2 + K_p s + K_i} \quad (1)$$

The AVR (automatic voltage regulator) maintains the nominal line to line RMS voltage of $415\ V$. The AVR present in the SG used is a frequency responsive PID controller, which was modelled according to the respective data-sheet [30]. The source impedance of the SG was found

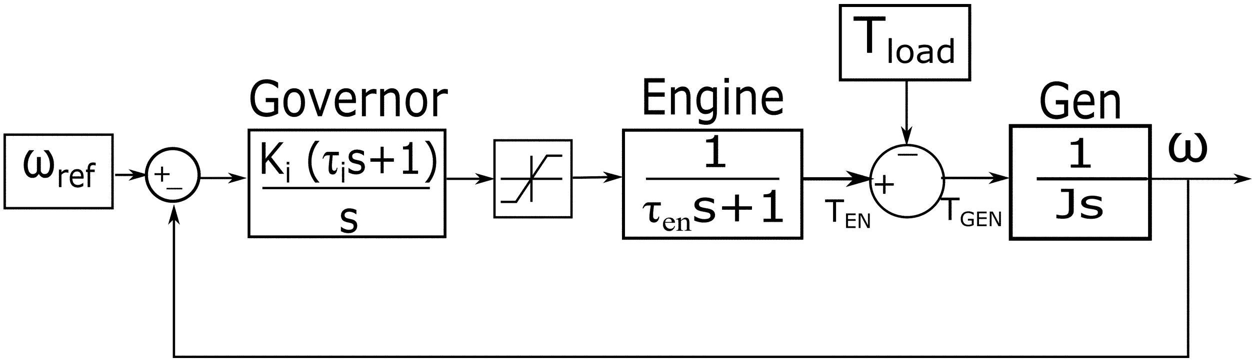

***Fig. 2.*** *The speed loop*

from the experimental rig to be $Z_s = 0.9 + j7.1\Omega$ by analysing the voltage and current characteristics during loading and shedding of resistive loads. As can be seen in Table 1, the inertia is relatively low, creating a weak grid environment that is susceptible to large frequency changes when loaded. The parameters of the weak grid used to design the speed controller for the prime mover are listed in Table 1, where friction $B$ was neglected for simplicity. The design has been carried out targeting a bandwidth of $1Hz$ and a phase margin of $40°$. The same model may be extended to represent multiple DGs with a droop control methodology for power sharing.

| **Parameter** | **Symbol** | **Value** |
|---|---|---|
| Generator Inertia | $J$ | $0.0447kgm^2$ |
| Engine time constant | $\tau_{en}$ | $38.1\ ms$ [31] |
| Speed loop proportional gain | $K_p$ | 0.1942 |
| Speed loop integral gain | $K_i = 5K_p$ | 0.9709 |
| Source impedance | $Z_s$ | $0.9 + j7.1\Omega$ |
| AVR Smoothing time constant | $\tau_{s(AVR)}$ | 20ms |
| AVR Exciter time constant | $\tau_{e(AVR)}$ | 11ms |
| AVR Generator field time constant | $\tau_{g(AVR)}$ | 780ms |
| Line Voltage | $V_{LL}$ | 400V |
| AVR phase margin | $PM_{AVR}$ | 65° |
| AVR rise time | $t_{r(AVR)}$ | 50ms |
| AVR damping factor | $\zeta_{AVR}$ | 0.707 |
| AVR proportional gain | $K_{p(PID)}$ | 39.1 |
| AVR integral gain | $K_{i(PID)}$ | 142 |
| AVR derivative | $K_{d(PID)}$ | 1.59 |

**Table 1** Parameters used in the simulated weak grid model.

## 3. Proposed Energy Storage Control Concept

The suitability of an ES technology for a given application depends mainly on its energy density, power density, and discharge duration. The technologies with higher power densities and shorter response times are more suitable for short-term frequency regulation within primary frequency control protocol [32, 33]. According to [34], primary short-term frequency response may last for less than 30 seconds and the secondary long-term frequency response may last for less than 30 minutes subsequent to a sudden generation loss. The aim of the proposed control system is to constrain the system frequency within $\pm 1Hz$ from the nominal $50Hz$ during load transients by injecting/absorbing short term active power during the transient. The frequency constraint of $49Hz - 51Hz$ was defined according to the normal operational frequency limits where continuous operation is required by power plants in the main utility grid as set by the grid code, UK [34]. This has been done without any communication between the prime mover and the ES.

### 3.1. Proportional ES Controller

Fig.3 shows the modified system with the ES control which incorporates a proportional controller. As can be seen, the frequency is detected and compared to the allowed deviation from the nominal $(1\ Hz)$, and this determines the control signal for the connected ES system. Initially it is assumed that the actual frequency of the system is available (i.e. we ignore the dynamics of the specific frequency detection method for the 'ideal' case), the frequency recovery that can be achieved by ES control is shown in Fig.4, where $K_{ES} = 30$. This figure is a qualitative representation of proposed power injection scheme: the procedure for designing the proportional gain $K_{ES}$ will be discussed later. When the frequency falls below the lower threshold $f^{l}_{th} = 49Hz$ the ES begins to supply active power proportional to the instantaneous frequency deviation from the threshold, so that the frequency is restored to $49\ Hz$ as shown in the Fig.4 when it switches off again. Throughout the load transient, the governor of the prime mover continues to act in parallel to the ES system: when the ES switches off, the governor reclaims full speed control, and restores the frequency to $50\ Hz$. An equivalent and opposite scenario occurs when the ES absorbs the excess power when load is shed and the system frequency rises above the upper threshold $f^{h}_{th} = 51\ Hz$. The equivalent torque $T_{ES}$ supplied by the ES can be mathematically expressed using $K_{ES}$ (the proportional gain),

$$T_{ES} = K_{ES} \begin{cases} f^{l}_{TH} - f & f < f^{l}_{TH} \\ 0 & f^{l}_{TH} < f < f^{h}_{TH} \\ f - f^{h}_{TH} & f > f^{h}_{TH} \end{cases} \tag{2}$$

The control system provides automatic activation and deactivation of the ES, based on the real-time estimate of system frequency, supplying active power only when frequency support is necessary. While the ES active power injection is taking place, the governor action creates a slow increase in the prime mover torque, and this will eventually remove the finite frequency error left once the ES switches off. The impact of the ES is to significantly reduce the frequency undershoot during a load impact (from $12\ Hz$ to $2\ Hz$ for the system considered) as can be seen in Fig. 4.

### 3.2. The Impact of Frequency Detection

It has been assumed that the ES support was triggered by direct measurement of system frequency. Practically, the frequency must be estimated by measuring and processing the voltage at the point of common coupling (PCC), via a dedicated frequency detection (FD) method. FD eliminates communication between the ES and the prime-mover to obtain the frequency data but introduces a transient delay and a steady state frequency ripple. A suitable trade-off must be identified in the choice of the FD method, since improving the transient response degrades the steady state response and vice-versa.

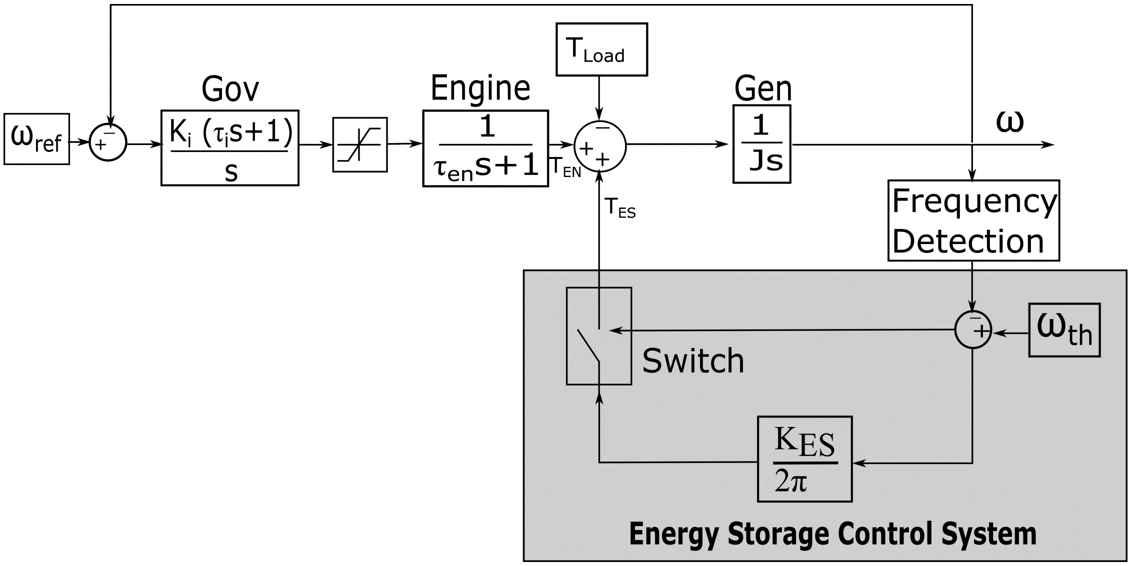

***Fig. 3.*** *Block diagram of the proportional ES control design*

*3.2.1. Transient Delay:* Fig.5(a) shows the effects of the FD time delay on the frequency recovery achieved for a rated load disturbance with the ES support using $K_{ES} = 30$. The ideal frequency signal was modified by adding a varying time delay representing varying FD delays of $10 - 40ms$ - corresponding to typical delays associated with common FD methods [35] . It can be concluded that the first order delay decreases the damping factor of the system for a fixed proportional gain $K_{ES}$, also increases the peak active power supplied as seen in Fig.5(b).

This phenomenon can also be viewed from a different perspective. The oscillations occur due to the high rate of injecting energy (power) proportional to the frequency drop. If the constant of proportionality $K_{ES}$ is decreased, one might be able to reduce the oscillations. Therefore, when the FD delay is increased, $K_{ES}$ needs to be limited to mitigate frequency oscillations. On the other hand, the maximum frequency drop in the recovered frequency increases with increased FD delay as seen in Fig.5(c). This may be of concern since a larger initial frequency dip crossing $47.5\ Hz$ may start load-shedding algorithms [34], thus reducing the effectiveness of the frequency support technique.

*3.2.2. Steady State Ripple:* Frequency mixing occurring in most FD techniques contributes towards a steady state ripple in the frequency estimate, which is mainly a double frequency component of the fundamental. A filtering technique is typically employed to eliminate the double frequency component and extract the fundamental in most FD methods.

In order to keep the investigation generic, a $100\ Hz$ ripple as added to the ideal frequency with varying ripple amplitudes [35, 36]. This frequency signal is fed into the ES controller and the frequency responses with ES support, for varying ripple amplitudes are shown in Fig.6(a). Even though all frequency signals switch the ES on, they switch the ES off at different times. Clearly, the higher the ripple amplitude, the larger the frequency deviation seen by the ES controller, and the higher the energy injected, thus, causing longer settling times. However, this causes the ES system to switch on and off frequently (at the frequency of the ripple). This also assumes that the ES can supply energy instantaneously.

Fig.6(b) shows that the total time for frequency recovery increases exponentially with increasing

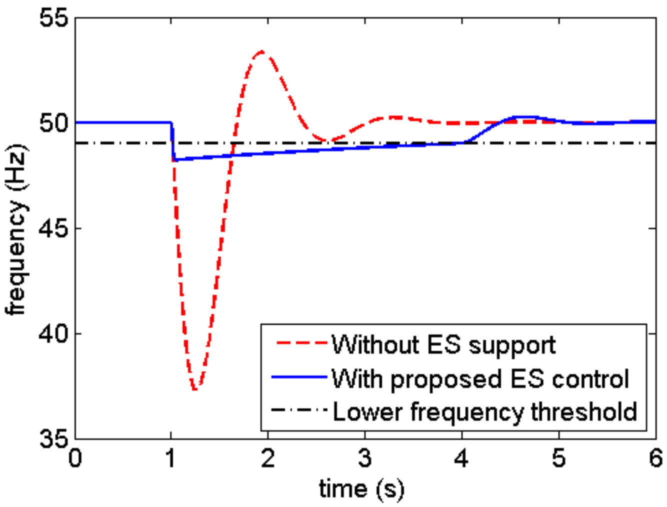

***Fig. 4.*** *The frequency response with and without ES control using an 'ideal' frequency input for a rated load disturbance*

ripple amplitude. Also, the peak active power from the ES increases linearly with increasing ripple amplitude as seen in Fig.6(b), suggesting that increasing the ripple amplitude increases the power converter requirements of the ES.

Referring to Fig.5(b), one can see that the peak power nearly doubles beyond a frequency detection delay of $50\ ms$. Hence, for this application $50\ ms$ was considered as the maximum transient response. A longer delay requires one to financially invest in a larger power converter. The discussion on the ripple amplitude suggests that even though it is theoretically possible to allow for ripple amplitude to be as large as $1\ Hz$ (more than $1\ Hz$ would never switch ES control off), $0.5\ Hz$ was taken as the requirement considering that a $50\ ms$ frequency detection delay would double the size requirement of the power units.

### *3.3. Detection of Frequency Following Load Transients*

Three candidate FD techniques were investigated namely. Synchronous Reference Frame PLL (SRF-PLL), Discrete Fourier Transform (DFT) and Double Second-Order Generalized Integrator Frequency Locked Loop (DSOGI-FLL). The DSOGI-FLL and the DFT were equally good compared to the SRF-PLL in detecting frequency, while meeting the requirements defined in the previous section. The design of the SRF-PLL and the DFT approach are well known [31, 35, 37], so only the specific design of the parameters for the DSOGI-FLL is presented in this paper. In this case, an empirical approach has been taken for the specific system considered to illustrate the specific effects the FLL has to deal with: a theoretical design approach will be presented in a future publication.

*3.3.1. Using DSOGI-FLL for Frequency Estimation:* The DSOGI structure consists of two second order generalised integrators (SOGI) with a quadrature signal generator(QSG) loop gain of $K$ [38]. The gain $K$ of QSG is set to $\sqrt{2}$ so that the transfer functions of the SOGI-QSG will have a damping factor $\zeta = \sqrt{2}$, delivering a compromise between the settling time and the overshoot.

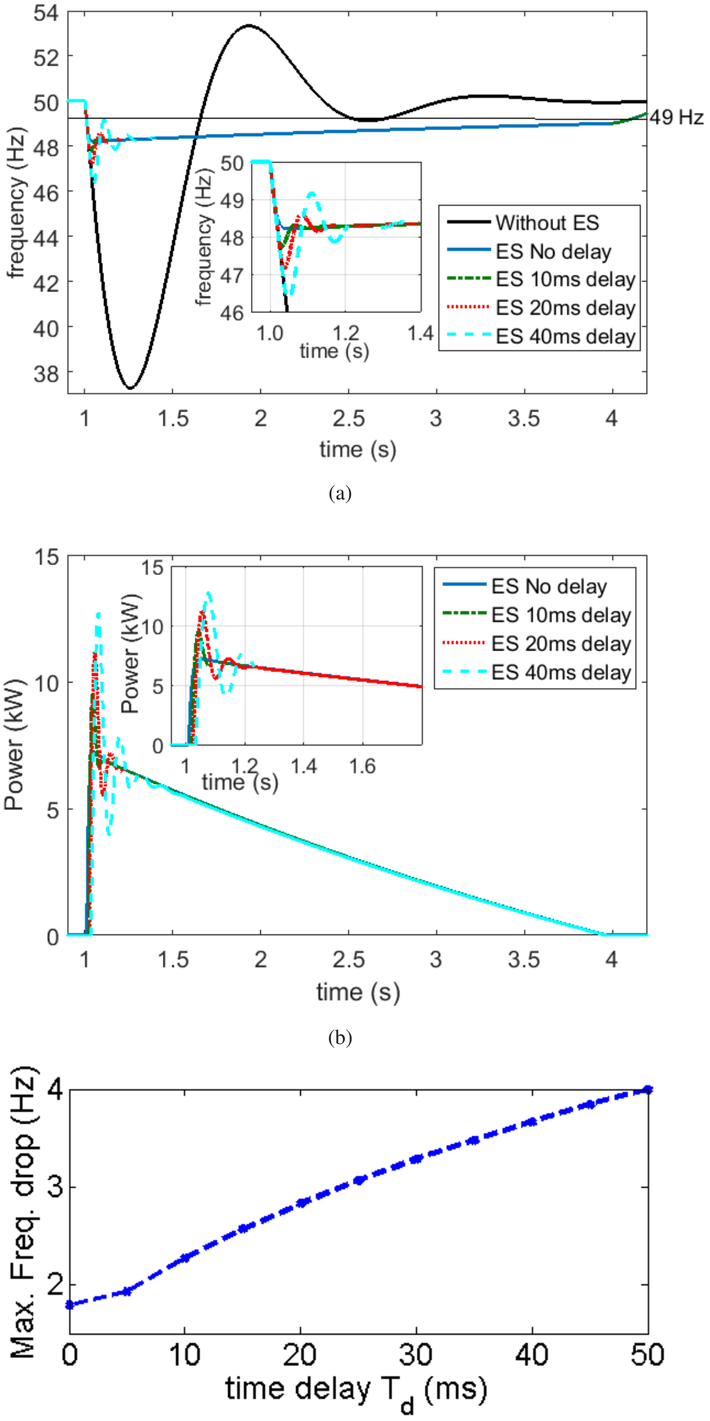

(a)

(b)

(c)

***Fig. 5.*** *The effect of frequency detection delay $T_d$ on (a) frequency recovery with and without energy storage, (b) active power supplied by the energy storage, (c) The effect of frequency detection delay $T_d$ on the maximum frequency drop with energy storage.*

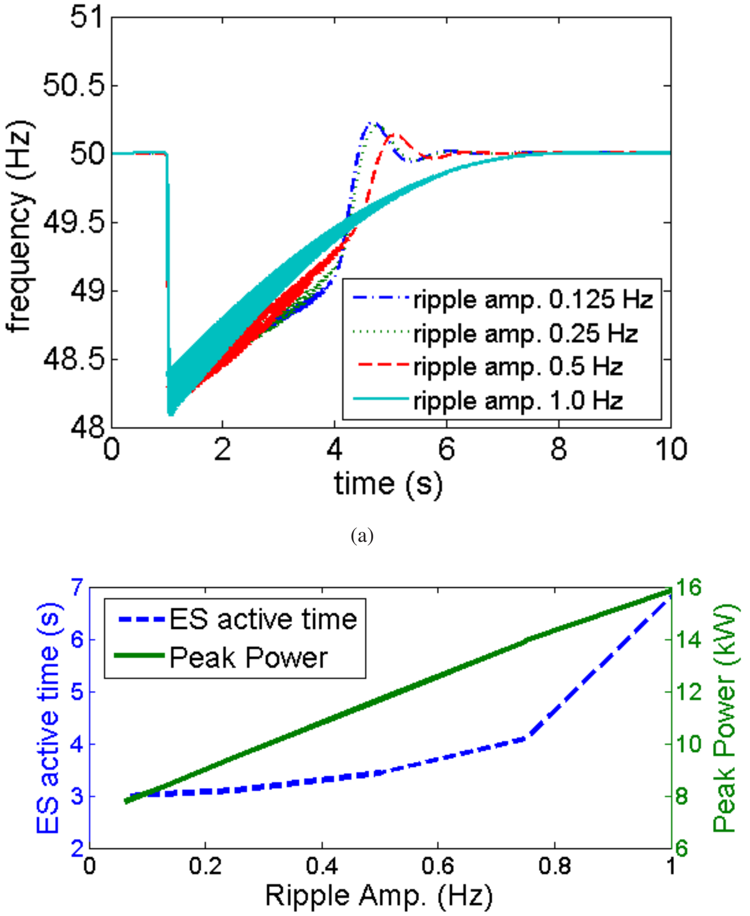

(a)

(b)

***Fig. 6.*** *The effect of frequency ripple with energy storage on (a) frequency recovery time and (b) active power supplied.*

According to [38] the settling time of the SOGI-QSG can be approximated by,

$$t_{s(SOGI)} = 3.9\tau,\ where\ \tau = \frac{2}{K\omega'} \tag{3}$$

where $\omega'$ is the angular frequency detected by DSOGI-FLL. This gives a settling time of $17.6ms$ for $50\ Hz$ for the QSG.

The gain of the FLL loop is $\Gamma$, which controls the overall settling time of the DSOGI-FLL. When $t_{s(FLL)} \geq 2\, t_{s(SOGI)}$, the FLL has a first-order response [35] and the settling time of the FLL system for a step frequency disturbance can be approximated to [39]

$$t_s(FLL) \approx \frac{3.9}{\Gamma} \tag{4}$$

*3.3.2. DSOGI-FLL response to ramp frequency:* An example of how the DSOGI-FLL estimates ramp frequency variations with a fixed delay is illustrated in Fig. 7(a) for a frequency ramp

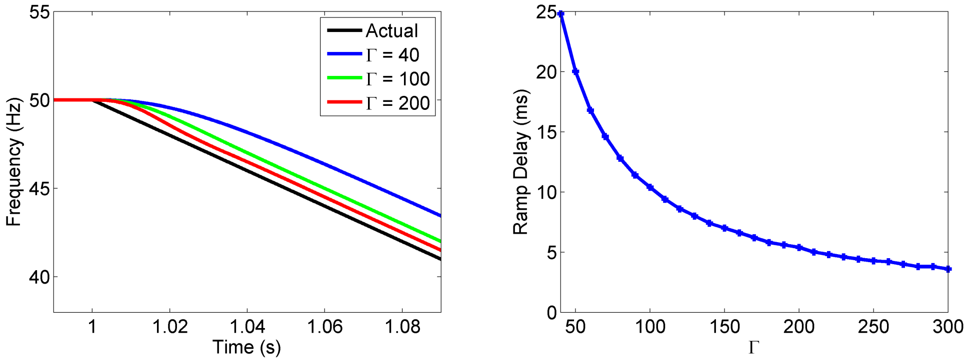

(a) (b)

***Fig. 7.*** *(a) Illustration of frequency detection for three illustrative* $\Gamma$ *for a ramp of* $100\ Hz/s$*, and (b) the detection delay for a* $100\ Hz/s$ *ramp with varying* $\Gamma$

of $100\ Hz/s$ for three different $\Gamma$ values. A ramp error is apparent, and is due to the use of only a single integrator – designed to eliminate the steady state error for a frequency step disturbance.

The ramp delay presented in Fig. 7(b) for various $\Gamma$ obtained for a frequency ramp of $100\ Hz/s$ shows an inverse relationship between the settling time and $\Gamma$. From the figure, one can see that the relationship is such that,

$$t_{s(ramp)} \approx \frac{1}{\Gamma} \tag{5}$$

To achieve a settling time of less than $50\ ms$ for a step frequency disturbance, $\Gamma > 78$ (from (4)) and to achieve a ramp delay of less than $50\ ms$, $\Gamma > 20$ (from (5)).

*3.3.3. DSOGI-FLL Response to Harmonics and Unbalance:* The effect when the input voltage was polluted with 6.07% THD and 5% voltage unbalance (estimated from the experimental MG when loaded) on the frequency detection by DSOGI-FLL is considered next.

The error of the detected frequency for a $2\ Hz/s$ ramp in the presence of harmonics and unbalances gives a measure of accuracy. Thus, the maximum error for the ramp between $40\ Hz$ and $60\ Hz$ for varying $\Gamma$ is shown in Figs.8(a) and 8(b) – separated into individual effects of harmonics and unbalance and combined effect respectively.

As seen in Fig.8(a), there is a finite error in the presence of unbalance. This is primarily due to the ramp delay error which reduces with increasing $\Gamma$. The ripple due to harmonics however increases with increasing $\Gamma$. From Fig.8(b), one can see that the combined error is approximately the same as the error due to harmonics. $\Gamma$ can now be restricted to $\Gamma < 125$ according to Fig.8(b), so that the error (ripple) is smaller than $0.2Hz$.

For the energy storage control system, the optimum value for $\Gamma$ was chosen to be $125$, in order to have minimum time delay without violating the required accuracy in the presence of voltage harmonics and unbalance.

*3.3.4. DSOGI-FLL Bandwidth Considerations:* The bandwidth of the DSOGI-FLL was considered next. The key to optimum dynamic response of a DSOGI-FLL is the proper selection of the proportional gain $K$ of the SOGI-QSG and the FLL gain $\Gamma$. Teodorescu et.al. in [35] suggest a first-order linearised frequency adaptive system to represent the DSOGI-FLL.

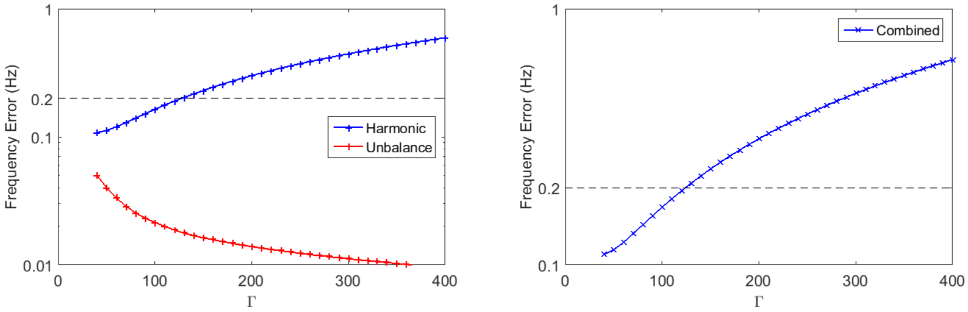

(a) (b)

***Fig. 8.*** *The frequency error of DSOGI-FLL in the presence of harmonics and unbalance for varying* $\Gamma$*, (a) Separate Errors (b) Combined Error*

In order to validate the linear approximation given in [35], a 3-phase balanced voltage signal without harmonic distortion or unbalance was considered. The step frequency response of the DSOGI-FLL was compared with a typical first order and a second order response. Using a regression analysis, the parameters of the most suitable first/second order system ($a$ in first order, $\zeta, \omega_n$ in second order) were selected. The DSOGI-FLL response and the obtained approximated system responses for $\Gamma = 200$ are shown in Fig. 9.

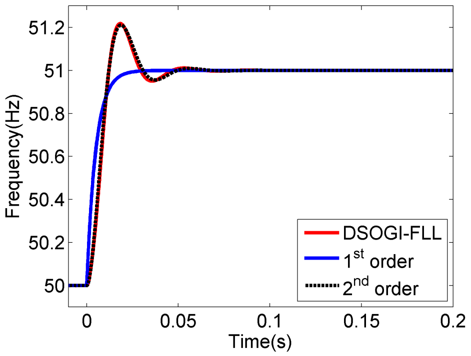

***Fig. 9.*** *Approximation of the DSOGI-FLL using first and second order systems for* $\Gamma = 200$

The results clearly show a discrepancy between the first order approximation and the actual response for higher values $\Gamma$ (i.e. 200) as shown in Fig.9. This is because as mentioned in [35] the first order approximation of DSOGI-FLL is only valid when the $t_{S(FLL)} \geq 2 * t_{S(SOGI)}$. From the settling times of the FLL, $t_{s(FLL)}$ for different $\Gamma$, calculated using (4), one can confirm that for higher $\Gamma$ this rule is violated.

The second order transfer function of the DSOGI-FLL is approximated for this design as,

$$\frac{\omega'}{\omega} = \left( \frac{\omega_n^2}{s^2 + 2\zeta\omega_n + \omega_n^2} \right) \tag{6}$$

where $\omega$ is the actual frequency and $\omega_n$ and $\zeta$ are the natural frequency and the damping factor of the DSOGI-FLL system [35]. Thus, the bandwidth of the DSOGI-FLL can be estimated by the following typical equation for bandwidth estimation for a second-order system.

$$\omega_{-3dB}(DSOGI - FLL) = \omega_n \left[1 - 2\zeta^2 + \sqrt{(2-4\zeta)^2 + 4\zeta^4}\right]^{1/2} \tag{7}$$

*3.3.5. Comparision of DSOGI-FLL with DFT and SRF:* For comparison, the bandwidth of a modified DFT [37] and a SRF-PLL [35] were derived using a similar approach to the DSOGI-FLL. A comprehensive derivation is available in [31]. The bandwidth of a modified DFT with a Blackman and Hamming windows was found to be,

$$w_{3dB(DFTHamming)} \approx \frac{4.5}{t_w} \tag{8}$$

$$w_{3dB(DFTBlackman)} \approx \frac{5.0}{t_w} \tag{9}$$

where $t_w$ is the DFT window length. The bandwidth of an SRF-PLL was derived using a second order system as [31],

$$\omega_{-3dB}SRF \approx \frac{1.185}{t_s} \tag{10}$$

where $t_s$ is the SRF-PLL settling time.

The comparison of the three methods for the same bandwidth when the DSOGI-FLL has a gain $\Gamma = 125$ is shown in Fig.10, where their response to the frequency change following a typical load change is shown. The parameters of the methods compared are shown in Table 2.

| **Method** | **Parameter** | **Value** |
|---|---|---|
| SRF-PLL | Settling Time ($t_s$) | $64.0\ ms$ |
| | Natural Frequency ($w_n$) | $86.2\ rad/s$ |
| DFT(Hamming) | Window length ($t_w$) | $25\ ms$ |
| DFT(Blackman) | Window length ($t_w$) | $29\ ms$ |
| DSOGI | $\Gamma$ | 125 |

**Table 2** Test case for comparison when the bandwidth is $177.4\ rad/s$

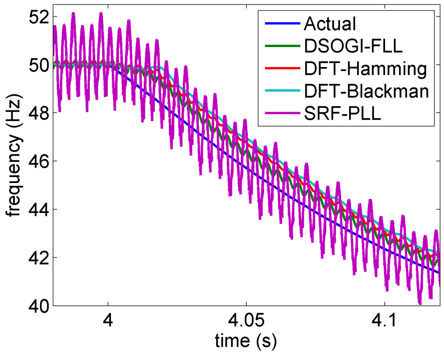

***Fig. 10.*** *Comparison of frequency detection techniques for the frequency trend following a load change*

As can be seen from Fig.10, the DSOGI-FLL shows the best estimation of the frequency trend with minimum delay and ripple. The DFTs suffer from a fixed delay determined by the window length whereas the SRF experiences a greater ripple at steady state, thus, making the both techniques less suitable for this application. The best DSOGI-FLL with the SOGI gain, $K = \sqrt{2}$ and the FLL gain, $\Gamma = 125$ settles within $40\ ms$ for a frequency step, has a ramp delay of $8\ ms$ and has a ripple amplitude of $\leq\ 0.2\ Hz$ for the harmonic content of the system voltage considered here [31].

Fig.11 shows an experimental comparison of the detected frequency using the implemented DSOGI-FLL along with the direct speed measurement from the induction motor drive used as the prime mover in the test system. The results show that using the detected frequency from the DSOGI-FLL method is as good as using the direct speed measurement from the motor drive, which also has an inherent measurement delay.

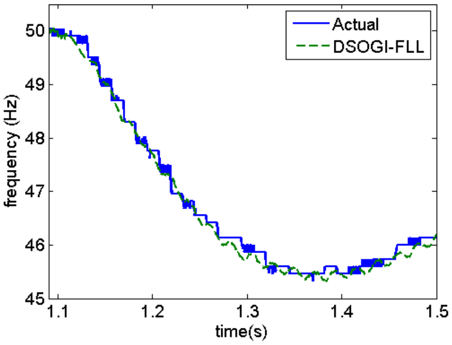

***Fig. 11.*** *Comparison of the DSOGI-FLL detected frequency with speed measured at the induction motor drive*

### *3.4. Influence of Electrical Components*

In the simulation studies, the proposed ES control was tested assuming that the ES acts as a torque equivalent to the required active power support at the PCC. In reality, the ES injects a current into the power system proportional to the frequency error.

The current is controlled to be in phase with the voltage and therefore is responsible for the active power injection. This was realised by means of a two stage power electronic converter with a bidirectional DC/DC converter and a 3-phase DC/AC inverter operating with current control employed in a rotating $dq$ frame of reference. The required active power, $P$ was injected as a d-axis current assuming that the required q-axis current is zero. The required d-axis current can be calculated using (11);

$$I_d = \frac{2\pi\ f_{DSOGI}\ T_{ES}}{V_d} = \frac{P}{Vd} \tag{11}$$

where $I_d$ and $V_d$ are the d-axis current required and the d-axis voltage at the PCC. $f_{DSOGI}$ is the frequency measured from the PCC voltage. The d-axis voltage $V_d$ is calculated by the Park-transformation using the phase of the 3-phase voltage estimated by the DSOGI-FLL.

Considering the large difference between the mechanical time constants that dominate the system under study and the control time constants of a current controlled converter, the total delay of the power conversion was modelled as a first order lag as given in (12),

$$Vs(s) = \frac{1}{\tau_v s + 1} \tag{12}$$

where the total vector control delay $\tau_v = 11\ ms$. This delay accounts for the total delay incurred between the generation of the equivalent torque demand from the control system and the supplying of the actual torque by the power converter. Even though the current controller has a smaller delay of $\approx 2\ ms$, the communication with the host interface implemented with a low bandwidth serial channel caused a more significant delay.

The complete electrical system introduces several non-linear components in to the system. This includes the d-axis voltage determination, the active power calculation, the d-axis current calculation and the 3-phase current injection. At each point, the control system has a non-linear dependence on both instantaneous voltage and instantaneous frequency rendering them critical to model.

While keeping the power conversion delay as a first order lag of $11\ ms$ in the system, the other effects caused by the source impedance and the AVR are lumped together as a pole-zero pair in the form of $\frac{\tau_b s+1}{\tau_c s+1}$. In order to determine the value of this pole-zero pair, an electrical system comprising the generator and the ES control was simulated alongside the LTI approximation shown in Fig.13 in Matlab/Simulink. Note that in the approximated system, the pole-zero pair is placed before supplying the ES torque ($T_{ES}$). By using a regression analysis, the torque equivalent of the injected power of the simulated electrical system was matched with the $T_{ES}$ of the approximated system after the pole-zero pair. The resulting $\tau_b, \tau_c$ was found to be $\tau_b = 0.0264\ s$ and $\tau_c = 0.114\ s$.

The pole-zero pair determined here is only valid for the specified impedance at the PCC, and the AVR of the generator. Even though these are characteristics of the host grid, they can be determined by an automated regression analysis to obtain an equivalent lumped LTI system transfer function. Therefore, this does not necessarily reduce the plug-and-play capabilities of the proposed ES control.

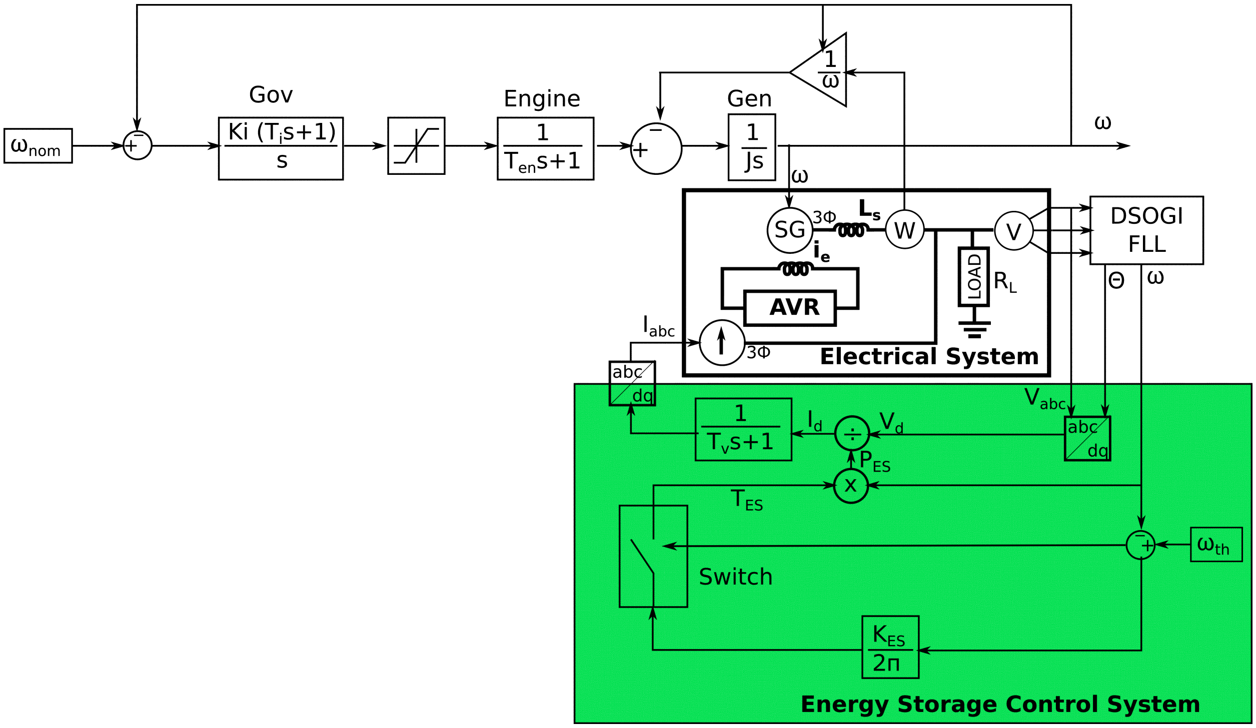

***Fig. 12.*** *Block diagram of the electrical system and control system of the weak grid with ES support, which is used in the simulations.*

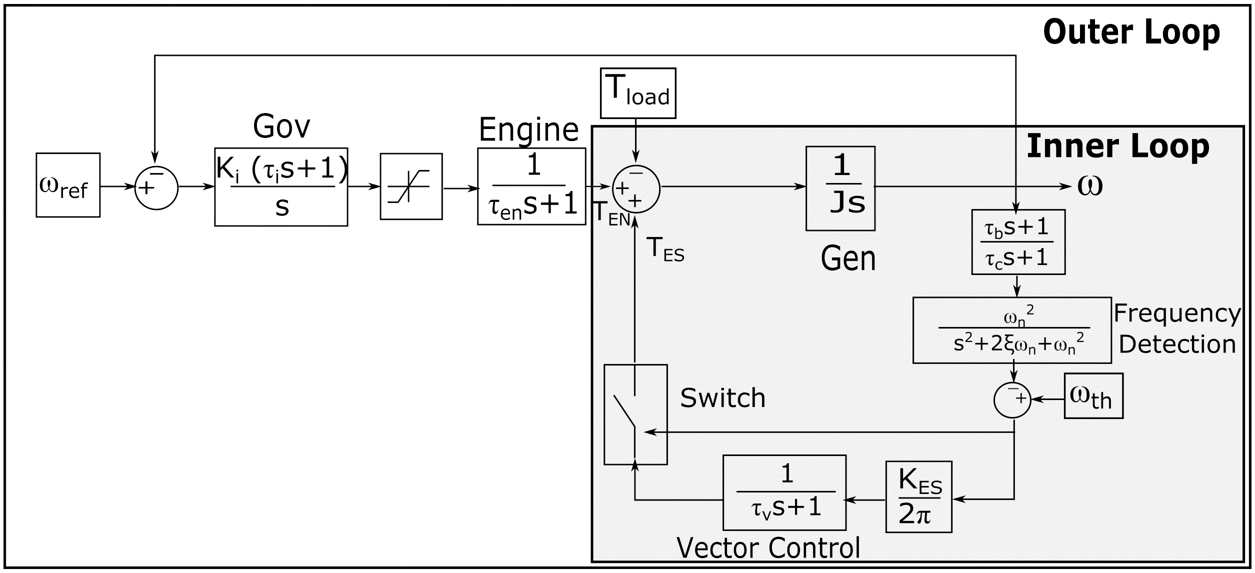

*Fig. 13.* *Block diagram of the LTI approximation of the weak grid with ES support.*

The equivalent control system for the complete weak-grid supported by the ES is shown in Fig.13, whereas the complete electrical and control system used for the simulations is shown in Fig. 12. In the complete electrical system, the speed governor loop of the generator remains unchanged. However, the load torque is now provided by dividing the measured power in the electrical system by the speed of the generator. The measured voltage is input to a DSOGI-FLL for frequency detection, which in turn is input to the energy storage control system. The ES control system outputs the torque required, which is then converted to a controlled current source, which provides active power to recover the frequency at the PCC. As can be seen, the control representations of the DSOGI-FLL frequency detection, the ES system with power conversion and other non-linear electrical characteristics are included in the weak grid control model. This model allows us to examine the stability of the ES control system alongside the weak grid simulation model and gives the complete scenario needed to design the proportional gain $K_{ES}$. Note that electrical load of the power system (and the ES system) are still approximated as torques acting on the prime mover in this system. This is reasonable since the power injected into the system at the PCC is equivalent to a reduction of torque load on the prime mover.

### 3.5. Stability Analysis of the ES Control

A root locus (RL) analysis was conducted on the approximated control system to identify the stability margins of the control technique as $K_{ES}$ varies. The approximated control system was taken as the two subsystems shown in Fig.13. The inner loop subsystem consists of the generator and the ES control feedback, whereas the outer loop subsystem includes the speed regulation. The inner loop must be faster than the outer one, and is therefore more critical for stability analysis.

The transfer functions of the forward control path and the feedback control path of the inner loop can be derived as,

$$\begin{aligned} \omega(s) &= \frac{1}{Js}(T_{EN}(s) - T_{ES}(s)) \qquad (13) \\ T_{ES}(s) &= \frac{K_{ES}}{2\pi}\left(\frac{\omega_n^2}{s^2 + 2\zeta\omega_n + \omega_n^2}\right)\left(\frac{\tau_b s + 1}{\tau_c s + 1}\right) \\ &\quad \left(\frac{1}{\tau_v s + 1}\right) \qquad (14) \end{aligned}$$

The RL of the inner loop for the open loop transfer function is shown in Fig.14(a). The two complex poles in the inner loop belong to the DSOGI-FLL. The most dominant poles start from the lumped pole and the pole at the origin belonging to the generator. The positions of the dominant poles crossing the imaginary axis are dependent on the location of the complex poles of the DSOGI-FLL.

The branches leave the stability region at $Gain \approx 70$. From (13) and (14), one can see that the *Gain* of the inner loop directly corresponds to the proportional gain $K_{ES}$.

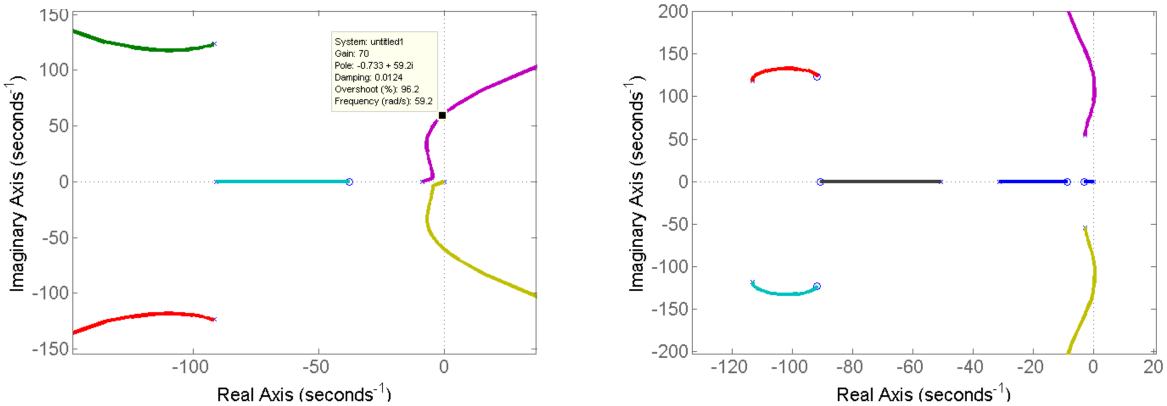

(a)

(b)

***Fig. 14.*** *The root locus of the (a) inner loop - generator and the energy storage and the (b) outer loop when* $K_{ES} = 60$

The overall system transfer function, including the PI speed governor and the prime mover transfer function is,

$$T_{EN}(s) = \left(\frac{K_i(\tau_i s + 1)}{s}\right)\left(\frac{1}{\tau_{en} s + 1}\right)(\omega_{ref} - \omega(s)) \qquad (15)$$

When $K_{ES} = 70$, the RL of the outer loop given by (15) becomes unstable for all gain values $K_i$. Therefore, for overall stability, $K_{ES}$ needs to be smaller than 70. For this particular system, the outer loop becomes marginally and unconditionally stable at $K_{ES} = 60$. The RL of the closed loop response of the overall system is shown in Fig.14(b), for $K_{ES} = 60$, i.e. $K_{ES}$ corresponding to the stability margin of the outer loop. Hence, one can conclude that the stability criterion for the overall system is $K_{ES} < 60$.

Simulations showing the frequency support using the approximated control system for different $K_{ES}$ values can be used to further verify the design. Figs.15(a) and 15(b) show frequency control responses carried out for a rated load disturbance when $K_{ES} = 40,\ 70$. As can be seen, the frequency response with $K_{ES} = 40$ (satisfies the stability criteria) had exponential damping, whereas when marginally unstable i.e. $K_{ES} = 70$, the frequency has sustained oscillations while the ES is active.

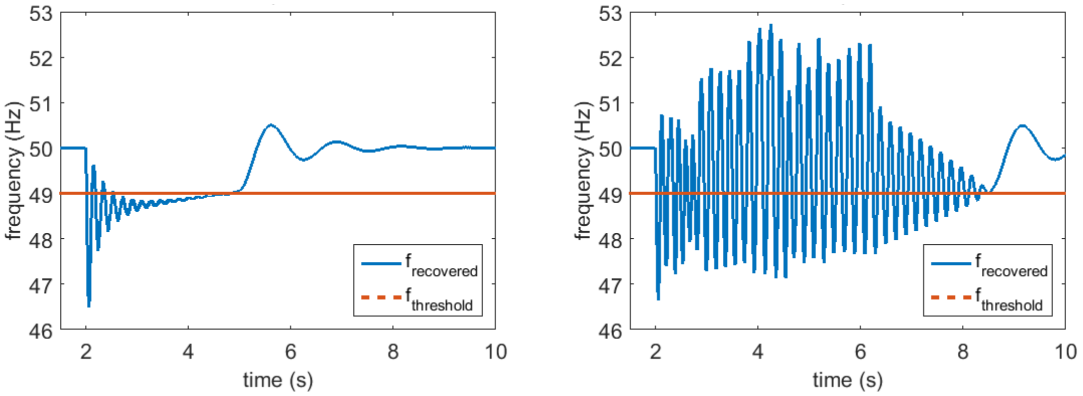

(a)

(b)

***Fig. 15.*** *The frequency response of the complete electrical system for ES gain* $K_{ES}$ *of (a)* $40$ *(stable) and (b)* $70$ *(unstable).*

To find any direct dependence of $K_{ES}$ on power system parameters, the CLTF of the inner loop was considered. From the inner loop system, one can write the characteristic equation as,

$$\begin{aligned} s(0.001s+1)(\tau_v s+1)(\tau_c s+1)(s^2+2\zeta\omega_n s+\omega_n^2) \\ +\frac{K_{ES}\omega_n^2}{2\pi J}(\tau_b s+1)=0 \end{aligned} \tag{16}$$

where the $(0.001s + 1)$ fast pole represents the filter required to suppress transients associated with contactor switching and parasitic circuit inductance. Thus, at the stability margin, the factor $K_{ES}/(2\pi J)$ will have a specific value depending on all other parameters $\omega_n, \zeta, \tau_v, \tau_c, \tau_b$. Of these parameters, $\omega_n, \zeta$ depend on the frequency detection technique, $\tau_v$ depends on the vector control, and $\tau_c, \tau_b$ depend on the electrical impedance and AVR effects in the system. When these parameters are fixed, $K_{ES}$ is directly proportional to system inertia $J$, meaning a system with higher inertia would allow the use of a higher $K_{ES}$ for the ES controller.

### 3.6. Current Limiting

In practice, the current is usually limited by the power converter used. Hence, limits are imposed on the current and on the peak power to replicate real world limitations. The maximum ES current will be mostly limited either by the maximum battery current or by the maximum converter current. The Li-ion BES used for the experimental system, which will be presented in the following section, was taken as an illustration. Current is not limited in the simulation results but the d-axis current was limited at $\pm 25A$ in the experimental rig.

## 4. Experimental Validation

The ES control with frequency detection was implemented using the same $8\ kW$ prototype MG introduced in Section 2. The generator is rated at $8\ kW$; its prime mover is a vector controlled induction motor drive with a short term peak power rating of 15 $kW$. A 24 $kWh/72\ Ah$ Lithium-ion battery with an operating voltage of $250V - 380V$ was used as the ES support system in the MG. The battery was connected to the grid using a 15 $kW$ Triphase PM15F42C AC-DC bidirectional power converter. The complete MG prototype used for the experiment is shown in Fig.16.

The load-side of the MG was configured with a resistive load connected via the 3-phase breaker C. Two 3-phase resistive loads equivalent to $57\Omega$ $(2.78kW)$and $27.5\Omega$ $(5.77kW)$ were used to create two test cases, representing a low power and a high power loading respectively. Thus, the maximum loading that could be achieved by the load bank available was 72% of the step load. A vector controlled induction motor drive was used to emulate the generator's prime mover.

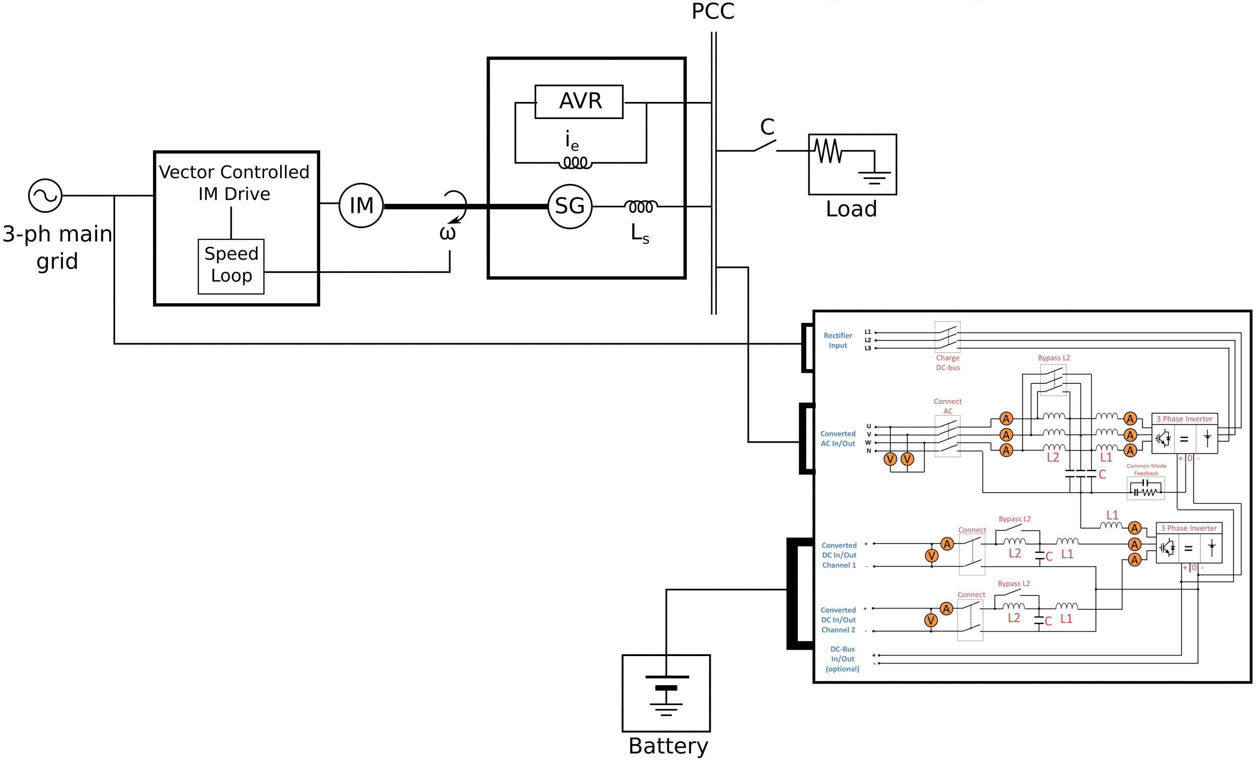

***Fig. 16.*** *Schematic of the experimental MG electrical connections [40]*

## 4.1. Frequency Support During Loading and Load Shedding

The experiment was conducted to observe the grid frequency, for load steps of 35% and 72% of generator rating with and without the proposed ES control. The speed of the generator available from the IM drive was recorded and is shown in Fig.17. Recovered frequency obtained by simulating the electrical system in Fig.12 is also shown in Fig.17. As can be seen, the frequency support achieved using the proposed control is clear in both cases when conducted with $K_{ES} = 30$. The value of $K_{ES} = 30$ was chosen so that the damped oscillations of the recovered frequency settle to less than $\pm 0.2\ Hz$ within $1\ s$. Also, the simulated frequency response matches with the experimental result reasonably well validating the simulation model derived.

### 4.1.1. Battery current, voltage and active power during loading:

In order to present the internal details of the experimental validation, the battery current drawn during loading is shown in Fig.18(a) and Fig.18(b). Since the battery is discharged during MG loading, the current recorded

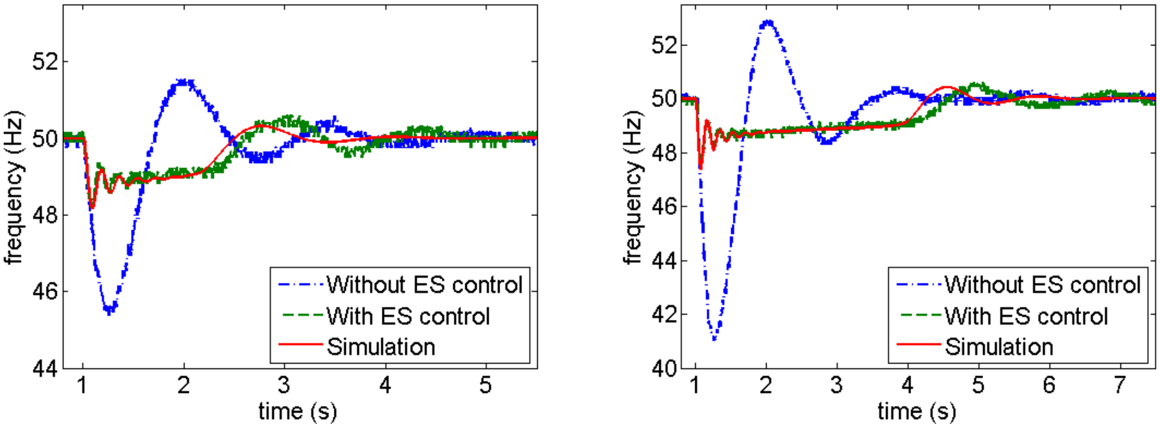

(a) (b)

***Fig. 17.*** *The frequency response of the experimental system compared with the simulated electrical system for ES gain* $K_{ES} = 30$ *for a) 0-35% step load b) 0-72% step load.*

is negative from the battery's perspective. The peak battery current and the duration of operation have both been increased proportional to the increasing loads. For the large load of $27.5\ \Omega$, the battery has supplied a maximum current of nearly $25\ A$ initially, which is close to the saturation limits (i.e. $\pm 25\ A$) imposed for the safe operation of the battery and the inverter.

The total active power supplied by the battery in both cases are shown in Fig.18(c) and Fig.18(d). For the $57\Omega$ load, the maximum power supplied was about $4.5kW$, whereas for $27.5\Omega$ it was increased to $8.5kW$ confirming the increase in the active power requirement from the battery.

An improvement in the voltage at the PCC due to ES support was also observed as shown in Fig.19. As mentioned earlier, the AVR of the generator is frequency responsive so that the amplitude of the 3-phase voltage reduces during large disturbances. This is more prominent for the 72% loading as shown in Fig.19(b). Both results illustrate the indirect improvement in voltage observed as a result of frequency support.

### *4.1.2. Load Shedding:*

In contrast to loading, the frequency can rise above $50Hz$ during load shedding. The BES can absorb the surplus power by means of charging; hence, with ES support, the frequency can also be successfully limited to $51Hz$, during load shedding.

A similar set of experiments were conducted in line with loading to observe the effectiveness of the energy storage in exploiting the surplus active power.

In Figs.20(a) and 20(b) , the frequency rises as high as $54Hz$ and $59Hz$ when shedding 37% and 72% of the rated active power without ES support, respectively. The longer oscillations observed in Fig.20(b) for the experiment compared to the simulation when shedding the larger load is due to the non-linear AVR effects competing with the power converter to stabilise grid voltage at nominal. In both cases, with the ES support the frequency could be successfully recovered at $51Hz$. The corresponding battery current and power supplied during the load shedding transient are shown in Figs.21(a) to 21(d).

The active power absorbed by the battery is shown in Fig.21(c),21(d) confirming the effective use of the energy storage, restricting the frequency from reaching higher levels. Neither of these cases show a drastic difference from that of loading and follows an acceptable general trend.

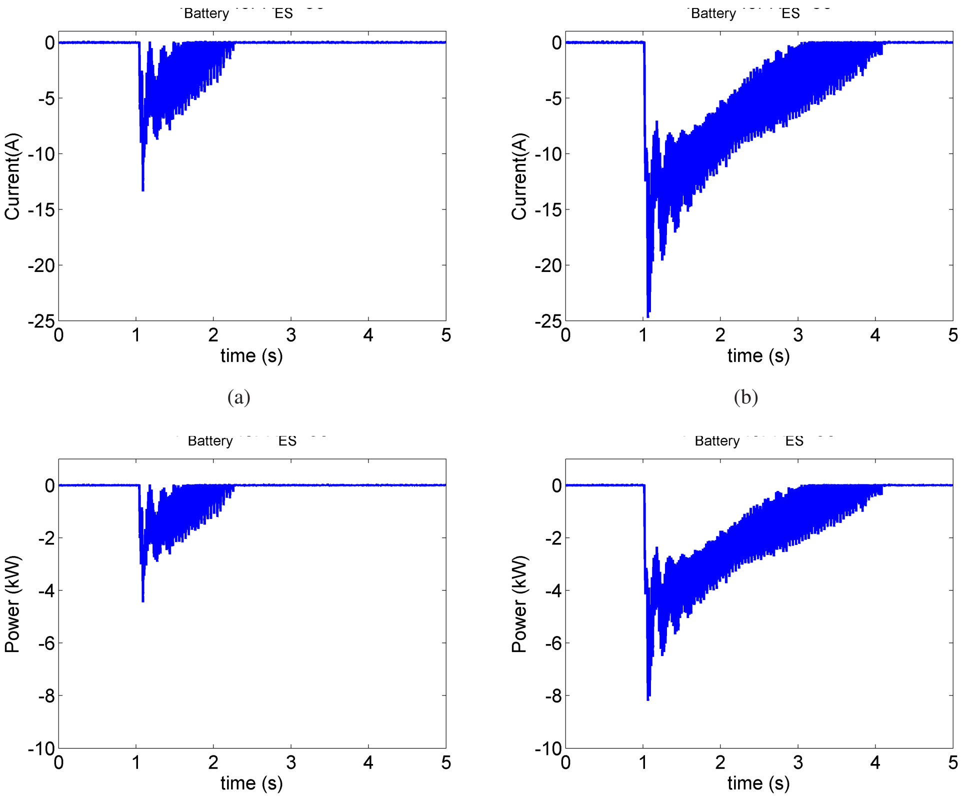

(a) (b)

(c) (d)

*Fig. 18. The current supplied by the battery energy storage to support frequency recovery a) 0-35% step load; b) 0-72% step load; The power supplied by the battery energy storage during frequency recovery c) 0-35% step load; d) 0-72% step load* $K_{ES} = 30$

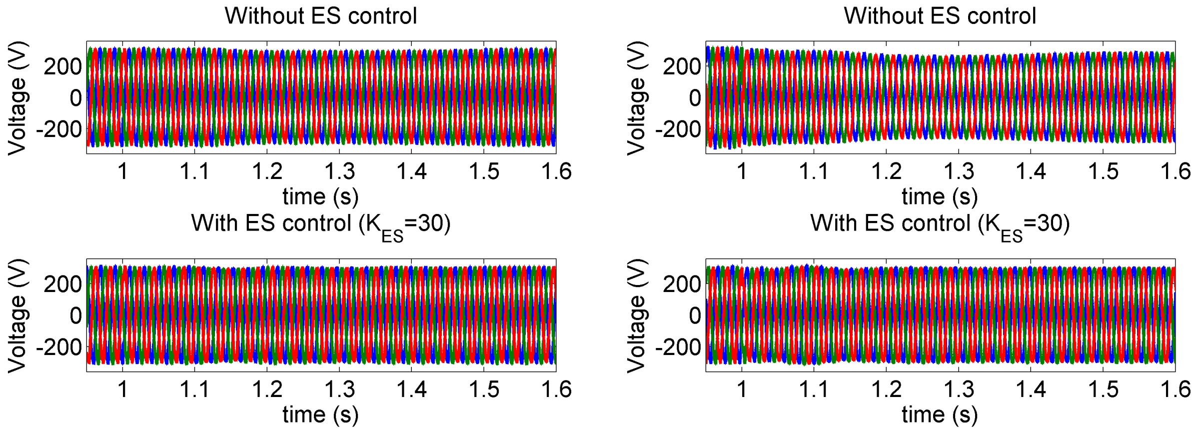

(a) (b)

*Fig. 19. The experimental voltage at the PCC with and without energy storage control during loading a) 0-35% step load b) 0-72% step load.*

## 4.2. Stability

The validity of the theoretical stability margin was demonstrated experimentally in the frequency responses for the loading of 35% and 72% of the generator rated power, when $K_{ES} = 50$, as shown

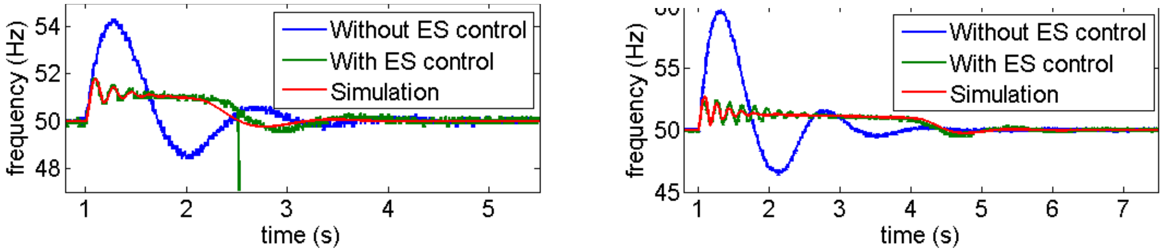

(a) (b)

*Fig. 20. Frequency support achieved by applying the proposed energy storage technique for load shedding a) 0-35% step load b) 0-72% step load.*

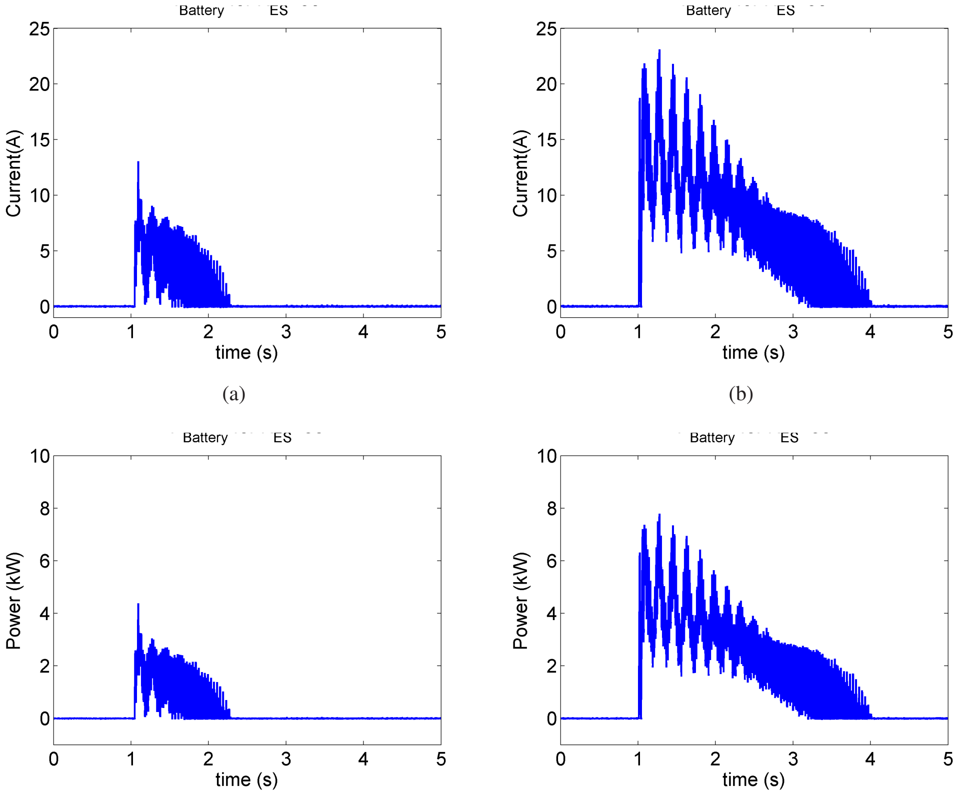

(c) (d)

*Fig. 21. The current absorbed by the battery energy storage during load shedding a) 0-35% step load; b) 0-72% step load; The active power absorbed by the battery energy storage during load shedding c) 0-35% step load; d) 0-72% step load* $K_{ES} = 30$

in Figs.22(a),22(b); and for when $K_{ES} = 70$, in Figs.22(c),22(d).

When $K_{ES}$ is changed from 30 to 50 there is an increase in the damped oscillations as expected confirming that the experimental system remains stable at $K_{ES} = 50$. When $K_{ES}$ was increased to 70 (Figs.22(c) and 22(d)), the experimental results show an oscillatory response with poor damping for both cases of loading. From the analysis in the previous sections, the theoretical stability margin of $K_{ES}$ was $K_{ES} = 60$. However, the difference in the simulated frequency recovery can be attributed to several sources. In addition to the approximations made while deriving the

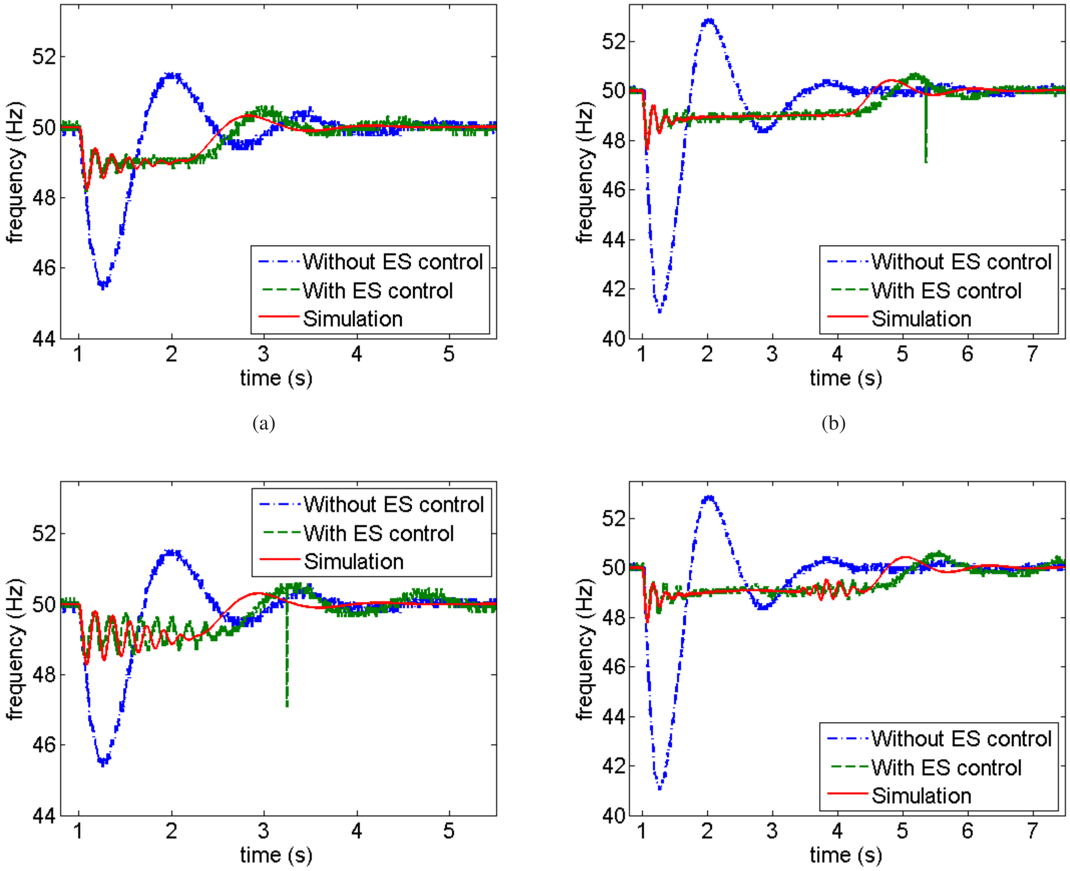

(a)

(b)

(c)

(d)

***Fig. 22.*** *The frequency response of the experimental system compared with the simulated electrical system for ES gain* $K_{ES} = 50$ *for a)* $35\%$ *loading b)* $72\%$ *loading; ES gain* $K_{ES} = 70$ *for c)* $35\%$ *loading d)* $72\%$ *loading*

equivalent transfer functions for control design, the different oscillations for $K_{ES} = 70$ in Fig.15 and Figs.22(c), 22(d) are due to the fact that the former was simulated without a current limit on the ES in place, while in the practical implementation current limiting introduces an equivalent attenuation in the control loop, giving margin for a higher $K_{ES}$. Friction in the system (neglected for simulation) will also damp oscillations. For these reasons, the proposed analytical design procedure can be seen as a worst case for the practical implementation.

## *4.3. Frequency Threshold*

The frequency support with tighter limits in ES control was investigated by setting the lower threshold to $49.5\ Hz$ (instead of $49\ Hz$). Figs.23(a) and 23(b) show the corresponding frequency support achieved for the $35\%$ and $72\%$ of the rated load experimentally, using $K_{ES} = 30$. As can be seen, increasing the threshold by $0.5\ Hz$ has successfully commanded the ES control to recover the frequency at the new threshold of $49.5\ Hz$. The oscillations are smaller in magnitude, but last about the same length of time when compared with Fig.17. Also, the maximum frequency error is lower. Due to the reduced speed-error available for the governor action, the settling of the overall

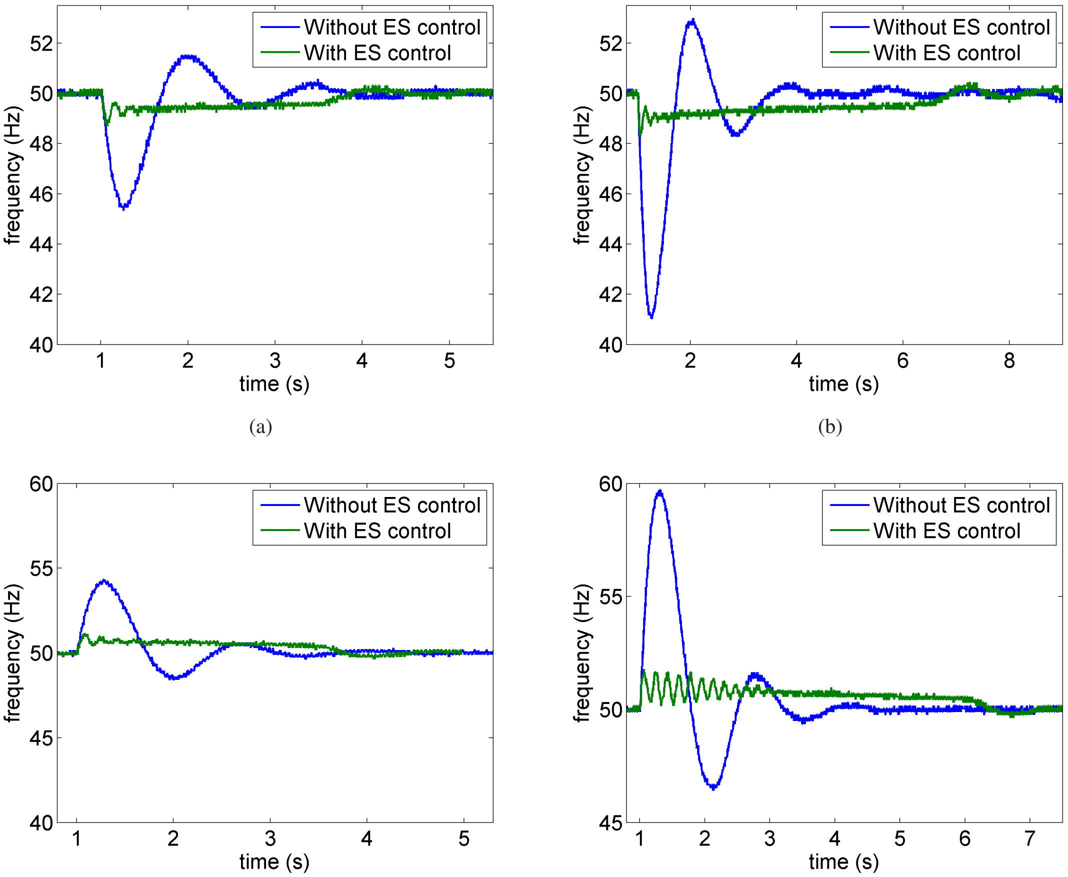

(a) (b) (c) (d)

***Fig. 23.*** *The frequency response of the experimental system compared with the simulated electrical system for ES gain* $K_{ES} = 30$ *and* $f_{TH} = 49.5\ Hz$ *with a)* $35\%$ *b) 72% loading; c)* $35\%$ *d) 72% load shedding;*

frequency response is lengthened compared to that when the threshold was $49\ Hz$. This is further elongated for the larger load as shown in Fig.23(b). Load shedding is presented Figs.23(c) and 23(d). The larger and longer oscillations observed in Fig.23(d) when shedding the larger load is due to the non-linear AVR effects as mentioned in load shedding (section 4.1.2).

Grid frequency regulations consider $1\%$ of the nominal ($\pm 0.5\ Hz$) as the normal operation limit for the frequency in the main utility grid according to Grid Code UK [34]. Therefore, the successful frequency support delivered by the proposed ES control for tighter frequency margins can be recognised for improved frequency regulation when required, especially in weaker sections of the grid.

## 5. Use of Multiple Energy Storage Systems and Prime Movers

Up to now, it was understood that the proposed energy storage can work independently from the prime mover. When multiple energy storage units operate, they all share the same frequency information. When the frequency thresholds are kept at the same value, the frequency difference between the instantaneous frequency and the threshold will be the same for all energy storage controllers. Since, power supplied is additive, $K_{ES}$ should also be added to come up with an effective $K_{ES}$ figure for the multiple energy storage systems.

To illustrate this, an electrical system with two energy storage units was simulated with a threshold $f_{TH} = 49\ Hz$, $K_{ES1} = 22.5$ and $K_{ES2} = 7.5$ in the two energy storage controllers. The frequency response of the dual storage system is shown in Fig. 24 along with the response of a single storage system with $K_{ES} = 30$ and $f_{TH} = 49\ Hz$ .

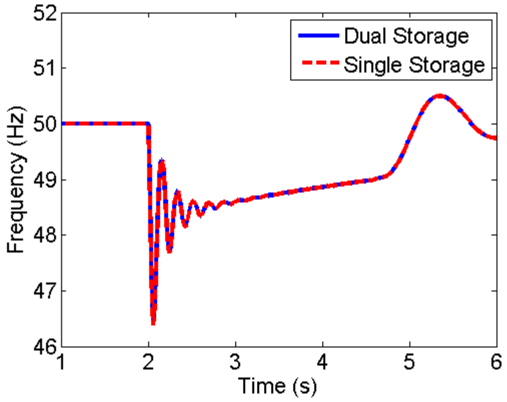

***Fig. 24.*** *The frequency variation of a dual storage system with* $K_{ES1} = 22.5$, $K_{ES2} = 7.5$ *and a single storage with* $K_{ES} = 30$, *while keeping* $f_{TH} = 49\ Hz$.

From Fig. 24, it can be seen that both systems provide equivalent frequency response: it appears that the effect of the ES systems are additive and their influence on the MG can be understood by adding their individual $K_{ES}$ values, when the frequency threshold of the energy storage control systems are the same.

In order to see the whether addition of $K_{ES}$ is still valid when combining energy storage units of different $f_{TH}$, two energy storage units with $K_{ES1} = K_{ES2} = 15$ were used with two thresholds $f_{TH1} = 49\ Hz$ and $f_{TH2} = 49.2\ Hz$. The resulting frequency response is shown in Fig.25 along with two simulations using single energy storage systems, one with $K_{ES} = 30$, $f_{TH} = 49\ Hz$ and the other with $K_{ES} = 30$, $f_{TH} = 49.2\ Hz$ for comparison.

According to Fig.25, one can see that the oscillations are the same for all three systems. Since $K_{ES}$ is the factor that affects the stability, one can conclude that all ES systems contribute to the overall $K_{ES}$ for the MG. The dual energy storage system, has a frequency control response which performs in between the single storage systems. Thus, the addition of individual $K_{ES}$ values still holds for systems with different thresholds, but the performance in every aspect (i.e. energy, power, frequency drop, and settling time) is in between what would occur for the single storage systems with corresponding frequency threshold values.

When multiple prime movers are connected to the same PCC, the energy storage systems can respond to the overall frequency variation, since the energy storage control is independent of prime mover governors. However, one should take care not to increase $K_{ES}$ beyond the stability value determined by the combined inertia $J$ of the two prime movers. Nonetheless, more theoretical and experimental work is required to assess the system performance in a droop controlled multiple prime mover, multiple energy storage system.

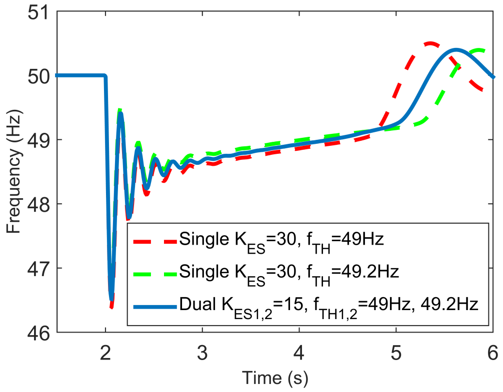

***Fig. 25.*** *The the frequency variation of two storage units with* $K_{ES1} = K_{ES2} = 15$, $f_{TH1} = 49\ Hz, f_{TH2} = 49.2\ Hz$ *and two single storage systems with* $K_{ES} = 30$, $f_{TH} = 49\ Hz$ *and* $K_{ES} = 30$, $f_{TH} = 49.2\ Hz$.

## 6. Conclusion

Weak electrical grids with distributed RES suffer from regular off-nominal frequency excursions during load disturbances due to low system inertia. Supplementing active power from fast-acting energy storage device is one way of offering power system frequency support. It can be considered as an equivalent to the kinetic energy stored in rotating masses (inertia) of the conventional distribution systems. This paper described a novel technique to automatically dispatch active power from a grid-connected ES to constrain frequency within $\pm 1Hz$ margins. This work identifies that supplying active power to support frequency to a level close to, but not equal to the nominal (i.e. a frequency threshold) is important, not only for the efficient use of the ES, but also for the unhindered operation of the speed governing of the power system to continuously supply the load in steady state. These properties were realised by exploiting detected power system frequency as the main control input to the ES control. This essentially eliminated the communication requirements between the prime mover and the ES control, but also improved the plug-and-play capabilities of the energy storage system. The complete system was validated in an experimental $8\ kW$ MG facility with a Li-ion BES.

## 7. References

[1] H. Bevrani, T. Ise, and Y. Miura, “Virtual synchronous generators: A survey and new perspectives,” *International Journal of Electrical Power & Energy Systems*, vol. 54, pp. 244–254, 2014.

[2] N. Jenkins, R. Allan, P. Crossley, D. Kirschen, and G. Strbac, *Embedded generation.* IEE, London, 2000.

[3] E. U. Committee, *The EU’s Target for Renewable Energy: 20 % by 2020.* EU, October 2008.

[4] J. A. R. Blanco, “How to manage the impact of distributed generation in the grid?” in *Integration of Renewables into the Distribution Grid, CIRED 2012 Workshop*, 2012, pp. 1–5.

[5] H. Laaksonen, “Protection principles for future microgrids,” *Power Electronics, IEEE Transactions on*, vol. 25, no. 12, pp. 2910–2918, 2010.

[6] N. Nimpitiwan, G. Heydt, R. Ayyanar, and S. Suryanarayanan, “Fault current contribution from synchronous machine and inverter based distributed generators,” *Power Delivery, IEEE Transactions on*, vol. 22, no. 1, pp. 634–641, 2007.

[7] H. Wan, K. K. Li, and K. Wong, “An adaptive multiagent approach to protection relay coordination with distributed generators in industrial power distribution system,” *Industry Applications, IEEE Transactions on*, vol. 46, no. 5, pp. 2118–2124, 2010.

[8] R. Lasseter, “Smart distribution: Coupled microgrids,” *Proceedings of the IEEE*, vol. 99, no. 6, pp. 1074–1082, 2011.

[9] N. Hatziargyriou, H. Asano, R. Iravani, and C. Marnay, “Microgrids,” *Power and Energy Magazine, IEEE*, vol. 5, no. 4, pp. 78–94, 2007.

[10] J. Kim, J. Guerrero, P. Rodriguez, R. Teodorescu, and K. Nam, “Mode adaptive droop control with virtual output impedances for an inverter-based flexible ac microgrid,” *Power Electronics, IEEE Transactions on*, vol. 26, no. 3, pp. 689 –701, March 2011.

[11] J. Guerrero, J. Vasquez, J. Matas, M. Castilla, and L. de Vicuna, “Control strategy for flexible microgrid based on parallel line-interactive ups systems,” *Industrial Electronics, IEEE Transactions on*, vol. 56, no. 3, pp. 726 –736, March 2009.

[12] E. Serban and H. Serban, “A control strategy for a distributed power generation microgrid application with voltage- and current-controlled source converter,” *Power Electronics, IEEE Transactions on*, vol. 25, no. 12, pp. 2981 –2992, Dec. 2010.

[13] C. Hernandez-Aramburo, T. Green, and N. Mugniot, “Fuel consumption minimization of a microgrid,” *Industry Applications, IEEE Transactions on*, vol. 41, no. 3, pp. 673 – 681, May-June 2005.

[14] P. Tielens and D. Van Hertem, “The relevance of inertia in power systems,” *Renewable and Sustainable Energy Reviews*, vol. 55, pp. 999–1009, 2016.

[15] S. DArco, J. A. Suul, and O. B. Fosso, “A virtual synchronous machine implementation for distributed control of power converters in smartgrids,” *Electric Power Systems Research*, vol. 122, pp. 180–197, 2015.

[16] J. W. Choi, S. Y. Heo, and M. K. Kim, “Hybrid operation strategy of wind energy storage system for power grid frequency regulation,” *IET Generation, Transmission & Distribution*, 2015.

[17] J. Liu, J. Wen, W. Yao, and Y. Long, “Solution to short-term frequency response of wind farms by using energy storage systems,” *IET Renewable Power Generation*, vol. 10, no. 5, pp. 669–678, 2016.

[18] I. Serban, R. Teodorescu, and C. Marinescu, “Energy storage systems impact on the short-term frequency stability of distributed autonomous microgrids, an analysis using aggregate models,” *IET Renewable Power Generation*, vol. 7, no. 5, pp. 531–539, Sept 2013.

[19] J. Muñoz-Cruzado-Alba, C. A. Rojas, S. Kouro, and E. Galván Díez, "Power production losses study by frequency regulation in weak-grid-connected utility-scale photovoltaic plants," *Energies*, vol. 9, no. 5, p. 317, 2016.

[20] H. Shi, F. Zhuo, H. Yi, F. Wang, D. Zhang, and Z. Geng, "A novel real-time voltage and frequency compensation strategy for photovoltaic-based microgrid," *IEEE Transactions on Industrial Electronics*, vol. 62, no. 6, pp. 3545–3556, 2015.

[21] H. Nikkhajoei and R. Lasseter, "Distributed generation interface to the certs microgrid," *Power Delivery, IEEE Transactions on*, vol. 24, no. 3, pp. 1598 –1608, July 2009.

[22] P. Kundur, *Power System Stability and Control.* McGraw-Hill, January 1, 1994.

[23] J.-Y. Kim, J.-H. Jeon, S.-K. Kim, C. Cho, J. H. Park, H.-M. Kim, and K.-Y. Nam, "Cooperative control strategy of energy storage system and microsources for stabilizing the microgrid during islanded operation," *Power Electronics, IEEE Transactions on*, vol. 25, no. 12, pp. 3037 –3048, Dec. 2010.

[24] B. Singh, J. Solanki, A. Chandra, and Kamal-Al-Haddad, "A solid state compensator with energy storage for isolated diesel generator set," in *Industrial Electronics, 2006 IEEE International Symposium on*, vol. 3, July 2006, pp. 1774 –1778.

[25] B. Singh and J. Solanki, "Load compensation for diesel generator-based isolated generation system employing dstatcom," *Industry Applications, IEEE Transactions on*, vol. 47, no. 1, pp. 238 –244, Jan.-Feb. 2011.

[26] A. Timbus, M. Liserre, R. Teodorescu, P. Rodriguez, and F. Blaabjerg, "Evaluation of current controllers for distributed power generation systems," *Power Electronics, IEEE Transactions on*, vol. 24, no. 3, pp. 654–664, 2009.

[27] T. Vandoorn, J. De Kooning, B. Meersman, and L. Vandevelde, "Review of primary control strategies for islanded microgrids with power-electronic interfaces," *Renewable and Sustainable Energy Reviews*, vol. 19, pp. 613–628, 2013.

[28] A. Agbedahunsi, M. Sumner, E. Christopher, A. Watson, A. Costabeber, and R. Parashar, "Frequency control improvement within a microgrid, using enhanced statcom with energy storage," 2012.

[29] P. M. Anderson and M. Mirheydar, "A low-order system frequency response model," *Power Systems, IEEE Transactions on*, vol. 5, no. 3, pp. 720–729, 1990.

[30] E. I. Automation, "Low voltage alternators - excitation and regulation systems shunt-pmg-arep," Leroy Somer, Tech. Rep., 2013.

[31] P. C. Jayamaha, "Energy storage for frequency support in weak electrical grids," Ph.D. dissertation, University of Nottingham, 2015.

[32] I. Wasiak, R. Pawelek, and R. Mienski, "Energy storage application in low-voltage microgrids for energy management and power quality improvement," *Generation, Transmission & Distribution, IET*, vol. 8, no. 3, pp. 463–472, 2014.

[33] I. Serban, R. Teodorescu, and C. Marinescu, "Energy storage systems impact on the short-term frequency stability of distributed autonomous microgrids, an analysis using aggregate models," *IET Renewable Power Generation*, vol. 7, no. 5, pp. 531–539, 2013.

[34] "The grid code," National Grid Electricity Transmission plc., Tech. Rep., 2014.

[35] R. Teodorescu, M. Liserre, and P. Rodriguez, *Grid converters for photovoltaic and wind power systems*. John Wiley & Sons, 2011, vol. 29.

[36] R. M. Santos Filho, P. F. Seixas, P. C. Cortizo, L. A. Torres, and A. F. Souza, "Comparison of three single-phase pll algorithms for ups applications," *Industrial Electronics, IEEE Transactions on*, vol. 55, no. 8, pp. 2923–2932, 2008.

[37] T. Lobos and J. Rezmer, "Real-time determination of power system frequency," *Instrumentation and Measurement, IEEE Transactions on*, vol. 46, no. 4, pp. 877–881, 1997.

[38] G. F. Franklin, M. L. Workman, and D. Powell, *Digital control of dynamic systems*. Addison-Wesley Longman Publishing Co., Inc., 1997.

[39] N. S. Nise, *CONTROL SYSTEMS ENGINEERING, (With CD)*. John Wiley & Sons, 2007.

[40] Triphase. (2015) Pm15f42c - 15kw power module with 3-phase + 2 ac/dc interface & 2 dc/dc interfaces. [Online]. Available: http://www.triphase.be/products/PM/15/F42